

1

2 **Physics-based characterization of soft marine sediments**3 **using vector sensors<sup>a)</sup>**4 **Oleg A. Godin<sup>b)</sup>**5  
6 *Department of Physics, Naval Postgraduate School, 833 Dyer Road, Monterey, California*  
7 *93943-5216, USA*8 **Thomas J. Deal**9 *Naval Undersea Warfare Center Division Newport, Newport, Rhode Island 02841, USA*10 **Hefeng Dong**11 *Department of Electronic Systems, Norwegian University of Science and Technology, 7491*  
12 *Trondheim, Norway*

13

14

15 Running title: Physics-guided geoacoustic inversion

16 Keywords: interface waves; shear rigidity; seismo-acoustic resonances; vector sensors;  
17 geoacoustic inversion18  
19 Submitted to the *Journal of the Acoustical Society of America* on July 13, 2020

20

21

---

<sup>a)</sup> Parts of this work have been previously reported at the 175<sup>th</sup> (Minneapolis, MN, May 2018) and 176<sup>th</sup> (Victoria, BC, Canada, November 2018) Meetings of the Acoustical Society of America

<sup>b)</sup> Electronic mail: oagodin@nps.edu

22 **Abstract**

23 In a 2007 experiment conducted in the northern North Sea, observations of a low-frequency  
24 seismo-acoustic wave field with a linear horizontal array of vector sensors located on the  
25 seafloor revealed a strong, narrow peak around 38 Hz in the power spectra and presence of  
26 multi-mode horizontally and vertically polarized interface waves with phase speeds between 45  
27 and 350 m/s. Dispersion curves of the interface waves exhibit piece-wise linear dependences  
28 between the logarithm of phase speed and logarithm of frequency with distinct slopes at large  
29 and small phase speeds, which suggests a seabed with a power-law shear speed dependence in  
30 two distinct sediment layers. The power spectrum peak is interpreted as a manifestation of a  
31 seismo-acoustic resonance. A simple geoacoustic model with a few free parameters is derived  
32 that quantitatively reproduces the key features of the observations. Our approach to the inverse  
33 problem is guided by a theoretical analysis of interface wave dispersion-and resonance reflection  
34 of compressional waves in soft marine sediments containing two or more layers of different  
35 composition. Combining data from various channels of the vector sensors is critical for  
36 separating waves of different polarizations and helps to identify various arrivals, check  
37 consistency of inversions, and evaluate sediment density.

38

39

40

41 PACS numbers: 43.30.Ma, 43.30.Dr, 43.30.Pc, 43.35.Pt

42

43 **I. INTRODUCTION**

44 Theoretical considerations,<sup>1, 2</sup> laboratory measurements,<sup>3</sup> and results of numerous field  
45 experiments<sup>4–16</sup> indicate that shear wave speed in granular materials and, in particular, in  
46 unconsolidated marine sediments increases with depth  $z$  below the seafloor and is approximately  
47 proportional to a certain power  $z^v$  of the depth as long as the composition of the materials  
48 remains unchanged. The power-law exponent  $v$  is probably controlled by the shape and  
49 roughness of the grains. The gradient of the shear wave speed (or shear speed, for brevity) is  
50 very large at small  $z$ , and the shear speed experiences large relative changes over several meters  
51 or tens of meters below the seafloor. Relative changes in density and compressional wave speed  
52 are much smaller, and these geoacoustic parameters can be modeled as depth-independent in a  
53 surficial layer of constant composition. Then, power-law depth-dependence of shear speed  
54 corresponds to the same power-law dependence on overburden pressure. Surficial  
55 unconsolidated sediments are “soft” in the sense that their shear rigidity and shear speed are  
56 small compared to the bulk modulus and compressional speed, respectively. For a more detailed  
57 discussion of the power-law depth-dependence of shear rigidity and additional references, see  
58 Refs. 2, 3, 17, and 18.

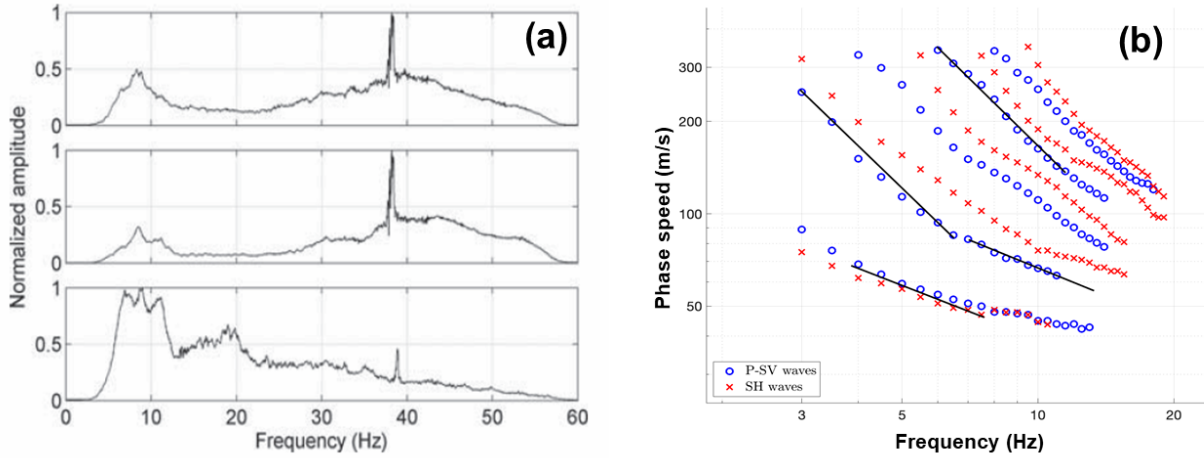
59 Soft sediments with power-law shear velocity profiles support horizontally, or  $SH$ , and  
60 vertically polarized, or  $P-SV$ , interface waves, which propagate along the seafloor with phase and  
61 group speeds of the order of the shear speed.<sup>10, 17</sup> These interface waves are slow in the sense that  
62 their phase and group speeds are small compared to the sound speed in water and compressional  
63 speed in the bottom. The vertically polarized seismo-acoustic interface waves are usually  
64 referred to as Scholte waves.<sup>19–22</sup> The dispersion and polarization properties of slow Scholte  
65 waves supported by soft sediments, shape functions of these waves, and wave energy distribution

66 between water and the seabed are all quite different from those of the Scholte waves that are  
67 supported by the interface of homogeneous fluid and solid half-spaces.<sup>23</sup> Moreover, dispersion  
68 properties of the vertically and horizontally polarized slow interface waves prove to be very  
69 similar,<sup>10, 17</sup> making vector sensors indispensable for identifying the wave types. The distinctive  
70 feature of the slow interface waves, which is readily recognized in their measured dispersion  
71 curves, is a power-law dependence of their phase and group speeds on frequency. There is a one-  
72 to-one correspondence between the exponents of the power laws for the frequency dependence  
73 of phase or group speeds and the depth-dependence of the shear speed.<sup>10, 17</sup> Observations of the  
74 interface waves are of considerable interest because their dispersion allows one to characterize  
75 geotechnical and geoacoustic parameters of surficial sediments that are difficult to measure by  
76 other means.<sup>7, 18–20, 24, 25</sup>

77 Vector sensors are increasingly employed in underwater acoustics to characterize seabed  
78 properties.<sup>26–28</sup> A rich dataset on wave propagation in the seabed<sup>29, 30</sup> was obtained in 2007 in the  
79 course of shear wave surveying of the Gjøa oil/gas condensate field in the North Sea off Norway,  
80 where a seabed-coupled mechanical vibrator generated probing signals in the frequency band  
81 from a few to 60 Hz. A long, densely populated linear array of three-component vector sensors  
82 was employed, which helped to separate vertically and horizontally polarized waves, identify a  
83 number of interface waves, and measure their phase speeds (Fig. 1). Measured dispersion curves  
84 of the interface waves have been inverted to retrieve the shear speed profile in the upper 4550  
85 meters of the seabed.<sup>22, 30</sup>

86 There are two striking features of the vector sensor data, which have not been previously  
87 explored. First, the vertical and radial components of the measured particle velocity have sharp  
88 peaks around 38 Hz (Fig. 1a), which suggest some kind of a seismo-acoustic resonance.<sup>9, 31, 32</sup>

89 Second, when plotted on the log-log scale, the dispersion curves of the interface waves exhibit  
 90 two distinct slopes at large and small phase speeds (Fig. 1b), which suggests that the seabed  
 91 contains layers with two different power-law profiles of the shear wave speed.<sup>7, 10, 17</sup> In this  
 92 paper, we re-examine the experimental results reported by Dong et al.<sup>22</sup> with the goal of  
 93 developing a simple, parsimonious geoacoustic model that qualitatively explains and  
 94 quantitatively reproduces the key features of the observations. Our approach to the inverse  
 95 problem is guided by a theoretical analysis of seismo-acoustic resonances and interface wave  
 96 dispersion in soft sediments containing two or more layers of different composition.



97

98 **Figure 1. (Color online)** Data of a 2007 experiment in the North Sea as processed by Dong et  
 99 al.<sup>22</sup> (a) Power spectra of the vertical particle velocity (top) and radial (middle) and cross-range  
 100 (bottom) components of the horizontal particle velocity. The spectra are averaged over seventy-  
 101 nine three-component vector sensors in a 390 m-long linear array. [Adapted from Fig. 3 in Ref.  
 102 22.] (b) Dependence of the phase speed  $u_n$  of interface waves on frequency. The phase speed  
 103 values retrieved by Dong et al.<sup>22</sup> from the experimental data are shown by crosses and circles and  
 104 plotted on log-log scale. The crosses and circles correspond to horizontally and vertically

105 polarized waves, respectively. Superimposed straight lines represent the power-law frequency  
106 dependencies with two different exponents (two black lines each).

107

108 The remainder of the paper is organized as follows. The experimental data underlying  
109 this work is described in Sec. II. Approximate analytic dispersion relations of interface waves  
110 supported by the seabed, which consists of two continuously stratified soft sediment layers  
111 overlaying a solid, homogeneous sub-bottom, are derived in Secs. 3A and 3B. The Wentzel–  
112 Kramers–Brillouin (WKB) approximation is employed in the derivation. The analytic dispersion  
113 relations are used in Sec. 3C to find a simple geoacoustic model consistent with the interface  
114 wave observations. A physical mechanism of resonant reflection of compressional waves by the  
115 seabed and geoacoustic implications of the observed resonant reflection are investigated in Sec.  
116 IV. The resulting geoacoustic model is compared to alternative models in Sec. V. Section VI  
117 summarizes our findings.

118

## 119 **II. EXPERIMENTAL DATA**

120 The data analyzed in this paper were acquired in a 2007 shear-wave survey<sup>29,30</sup> of the Gjøa field  
121 located in the Norwegian Channel in the northern North Sea off the southern coast of Norway.  
122 The water depth at the experiment site was 364 m, and the main geological interfaces at the site  
123 are flat. Surficial sediment layers are composed of soft Holocene clays deposited on glacial and  
124 glacio-marine sediments.<sup>29,30</sup> A massive seabed-coupled vibrator generated the seismo-acoustic  
125 wave field. The wave source was developed by the Norwegian Geotechnical Institute to  
126 efficiently generate low-frequency shear waves of different polarizations; limited compressional  
127 waves were also radiated by the source.<sup>29,30</sup> The frequency content of the probing signals

128 generated by the source was approximately from 2 to 60 Hz with a broad maximum around 37  
129 Hz and width of about 20 Hz at half-power level, see Fig. 5 in Ref. 29.

130 The signals were received on a one-kilometer-long ocean-bottom cable (OBC), which  
131 was deployed partially in water and partially on the seafloor in a radial direction from the source.  
132 The OBC contained 42 three-component accelerometers with 25 m spacing. To improve the  
133 resolution of short waves, a 600 m-long synthetic aperture with a much shorter 2.5 m receiver  
134 spacing was created by dragging the cable in 2.5 m steps.<sup>29</sup> Orientations of the three orthogonal  
135 receiver components were determined using airgun signals and used to represent the data in  
136 terms of the vertical and in-line (radial) and cross-range (tangential) horizontal components. This  
137 proved critical for proper discrimination and identification of various arrivals within the complex  
138 full field data.<sup>22, 29, 30</sup> Assuming a horizontally stratified seabed, the cross-range particle velocity  
139 is due to horizontally polarized (*SH*) shear waves, while radial and vertical components of the  
140 particle velocity are due to vertically polarized (*SV*) shear waves and compressional (*P*) waves.  
141 Detected arrivals included head waves, multiply reflected shear waves, and at least ten modes of  
142 horizontally and vertically polarized interface, or surface, waves.<sup>22, 29, 30</sup>

143 Interface waves were observed at frequencies from about 2 to 20 Hz. Dispersion curves  
144 of the horizontally polarized interface waves have been extracted from the cross-range  
145 components of particle acceleration measured on the synthesized aperture horizontal array, while  
146 dispersion curves of the vertically polarized interface waves have been measured using the  
147 vertical and radial components of the acceleration.<sup>22, 30</sup> The dispersion curves are illustrated in  
148 Fig. 1b. The interface wave dispersion curves have been previously inverted by Socco et al.<sup>30</sup> and  
149 Dong et al.<sup>22</sup> to retrieve the depth dependence of the shear wave speed in the top 40–50 m of the  
150 seabed. The seabed was modeled as a stack of homogeneous layers in these inversions.

151 Because of limitations on access to proprietary raw data, this paper focuses on re-analysis  
152 of the previously published<sup>22, 29, 30</sup> information on interface wave dispersion and power spectra of  
153 signals recorded by the three-component vector sensors. Available data consists of the frequency  
154 dependence of the phase speed of various interface waves (Fig. 1b), as retrieved by Dong et al.,<sup>22</sup>  
155 and power spectra of the vertical, radial, and cross-range components of the full field. The power  
156 spectra<sup>22</sup> averaged over multiple receivers and repeatedly emitted probing signals are shown in  
157 Fig. 1a. For each of the vertical, radial, and cross-range components of particle velocity, the  
158 average power spectra are normalized by their respective maxima.

159 The main maxima of the power spectrum of the cross-range component of the field are at  
160 frequencies below 20 Hz (Fig. 1a). In addition to broad low-frequency peaks below 10 Hz, which  
161 are associated with vertically polarized interface waves, the power spectra of the vertical and in-  
162 line components have significantly larger, narrow peaks around 38 Hz. (A much smaller peak at  
163 a similar frequency in the spectrum of the cross-range component is probably due to imperfect  
164 separation of the measured acceleration into the vertical, radial, and cross-range components  
165 resulting from uncertainties in the measurements of spatial orientation of individual vector  
166 sensors.) These sharp peaks are suggestive of a resonance phenomenon occurring in either the  
167 experimental equipment or the environment. In particular, as already mentioned, the source  
168 spectrum is maximum at about 37 Hz. However, the bandwidth of the source spectrum at half-  
169 power is at least 20 times larger than the sub-1 Hz width of the spectral peaks of the wave field  
170 (Fig. 1a). We interpret the sharp spectral peaks around 38 Hz as a seismo-acoustic resonance  
171 originating from wave propagation conditions at the experimental site. It is shown in Secs. IV  
172 and V that such an interpretation is consistent with available geological information and results  
173 of inversion of the interface wave data.

174

175 **III. INTERFACE WAVES**176 **A. Asymptotic dispersion relations of horizontally polarized interface waves**

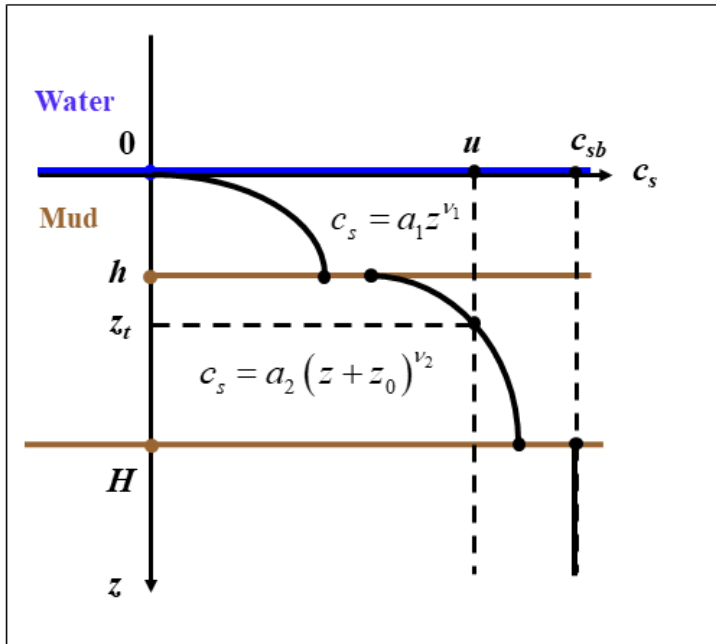
177 Consider a model of soft marine sediments (Fig. 2), which consists of two layers with power-law  
 178 shear velocity profiles:

179  $c_s(z) = a_1 z^{\nu_1}, \quad 0 < z < h,$  (1)

180  $c_s(z) = a_2 (z + z_0)^{\nu_2}, \quad h < z < H.$  (2)

181 The layers are located between the water column at  $z < 0$  and a homogeneous solid half-space  
 182 (subbottom) at  $z > H$ . Here  $h$  is the thickness of the upper sediment layer, and  $H$  is the vertical  
 183 extent of the soft sediments. Physical considerations and available observations indicate that  
 184  $0 \leq \nu_{1,2} < 1$ .<sup>9, 10, 17</sup> Shear and compressional wave speeds and density in the subbottom are  $c_{sb}$ ,  $c_{lb}$ ,  
 185 and  $\rho_b$ , respectively. Sound speed and density of water near the seafloor are  $c_w$  and  $\rho_w$ ;  
 186 compressional wave speeds and densities in respective sediment layers are  $c_{l1}$ ,  $\rho_1$  and  $c_{l2}$ ,  $\rho_2$ . For  
 187 simplicity, we assume that variations of the sediment density and compressional wave speed are  
 188 negligible within each soft sediment layer. We will also assume that shear speed increases  
 189 steadily with depth, which implies  $a_1 h^{\nu_1} \leq a_2 (h + z_0)^{\nu_2}$  and  $a_2 (H + z_0)^{\nu_2} \leq c_{sb}$ .

190



191

192 **Figure 2. (Color online)** Depth dependence of the shear wave speed  $c_s$  in the seabed. Two soft  
 193 sediment layers  $0 < z < h$  and  $h < z < H$  with power-law depth dependencies overlie a  
 194 homogeneous solid subbottom.

195

196 The increase of the shear speed  $c_s$  with depth below the seafloor creates a waveguide for  
 197 shear waves. Horizontally polarized (*SH*) interface waves are normal modes of this waveguide.  
 198 Despite the simplicity of the geoacoustic model, the wave equation cannot be solved analytically  
 199 in terms of known mathematical functions for arbitrary values of exponents  $v_1$  and  $v_2$ .<sup>9, 17</sup> We  
 200 will use a WKB-based asymptotic approach to derive the dispersion relation of the interface  
 201 waves. Disregarding reflection at the interface  $z = h$ , the normal mode dispersion equation can be  
 202 written as follows in the WKB approximation:<sup>23</sup>

203 
$$V_1 V_2 \exp(2i\omega\varphi(z_{lb})) = 1, \quad \varphi(z_{lb}) = \int_0^{z_{lb}} \sqrt{c_s^{-2}(z) - u^{-2}} dz. \quad (3)$$

204 Here  $\omega$  stands for wave frequency,  $V_1$  and  $V_2$  are plane-wave reflection coefficients at the upper,  
 205  $z = 0$ , and lower,  $z = z_{lb}$ , boundaries of the waveguide. The lower boundary is either the turning  
 206 point  $z = z_t$ , where shear speed equals the phase speed  $u$  of the normal mode:  $c_s(z_t) = u$ , or the  
 207 lower boundary  $z = H$  of the soft sediment, if there are no turning points. Note that the phase  
 208 integral steadily increases with  $u$ .

209 Introducing a new integration variable,  $w = u^2/c_s^2 - 1$ , reduces the phase integral  $\varphi(z)$  in  
 210 any layer with a power-law dependence of  $c_s$  to

$$211 \quad \varphi(z_{lb}) = \frac{-1}{vu} \left( \frac{u^2}{a} \right)^{1/\nu} \int_{w(0)}^{w(z_{lb})} w^{1/2} (w+1)^{-1-1/\nu} dw.$$

212 This is a standard integral [see, e.g., Eq. (1.2.4.3) in Ref. 33], which can be expressed in terms of  
 213 a hypergeometric function<sup>34</sup> for arbitrary integration limits but simplifies when one of the limits  
 214 is either  $w = 0$  or infinity. Note that  $w = 0$  at the turning point  $z = z_t$  and  $w \rightarrow +\infty$  when  $z \rightarrow 0$ .

215 All normal modes are evanescent waves in the subbottom and have phase speeds  $u < c_{sb}$ .  
 216 When  $0 < u < a_1 h^{\nu_1}$ , the turning point  $z = z_t$  of the wave is located in the upper sediment layer at  
 217  $z_t = (u/a_1)^{1/\nu_1}$ . Then, integration is over the semi-infinite interval  $0 < w < +\infty$  in the phase  
 218 integral, and we obtain

$$219 \quad \varphi(z_t) = \frac{u^{-1+1/\nu_1}}{a_1^{1/\nu_1}} \frac{\sqrt{\pi} \Gamma((1-\nu_1)/2\nu_1)}{2\Gamma(1/2\nu_1)} \quad (4)$$

220 in agreement with Ref. 17. Here  $\Gamma(\cdot)$  is Gamma function, see Chap. 6 in Ref. 34.

221 When  $a_1 h^{\nu_1} \leq u \leq a_2 (h+z_0)^{\nu_2}$ , integration in the phase integral is from  $z = 0$  to  $z = h$ . The  
 222 latter corresponds to a finite value of  $w$ . Using Eq. (1.2.4.3) in Ref. 33, we find

223 
$$\varphi(h) = \frac{u^{-1+\nu_1}}{a_1^{\nu_1}} \left[ \frac{\sqrt{\pi} \Gamma((1-\nu_1)/2\nu_1)}{2\Gamma(1/2\nu_1)} - \frac{1}{3\nu_1} \left( \frac{u^2}{a_1^2 h^{2\nu_1}} - 1 \right)^{3/2} F \left( \frac{3}{2}, 1 + \frac{1}{2\nu_1}; \frac{5}{2}; 1 - \frac{u^2}{a_1^2 h^{2\nu_1}} \right) \right]. \quad (5)$$

224 Here  $F(A, B; C; D)$  is the hypergeometric function, also known as the Gauss hypergeometric  
225 series or  ${}_2F_1(A, B; C; D)$  hypergeometric function, see Chap. 15 in Ref. 34.

226 When  $a_2(h+z_0)^{\nu_2} < u < a_2(H+z_0)^{\nu_2}$ , the wave has a turning point at  $z_t = (u/a_2)^{\nu_2} - z_0$   
227 within the lower sediment layer. Then, the phase integral is a sum of the integral in the upper  
228 sediment layer, which is given by Eq. (5), and an integral over  $h < z < z_t$  in the lower sediment  
229 layer. Similar to derivation of Eq. (5), we obtain

230 
$$\varphi(z_t) = \varphi(h) + \frac{u^{-1+\nu_2}}{3\nu_2 a_2^{\nu_2}} \left( \frac{u^2}{a_2^2 (h+z_0)^{2\nu_2}} - 1 \right)^{3/2} F \left( \frac{3}{2}, 1 + \frac{1}{2\nu_2}; \frac{5}{2}; 1 - \frac{u^2}{a_2^2 (h+z_0)^{2\nu_2}} \right). \quad (6)$$

231 Finally, when  $a_2(H+z_0)^{\nu_2} \leq u < c_{bs}$ , there are no turning points, and the phase integral is given  
232 by

233 
$$\varphi(H) = \varphi(h) + \frac{u^{-1+\nu_2}}{3\nu_2 a_2^{\nu_2}} \left[ \left( \frac{u^2}{a_2^2 (H+z_0)^{2\nu_2}} - 1 \right)^{3/2} F \left( \frac{3}{2}, 1 + \frac{1}{2\nu_2}; \frac{5}{2}; 1 - \frac{u^2}{a_2^2 (H+z_0)^{2\nu_2}} \right) \right. \\ \left. - \left( \frac{u^2}{a_2^2 (h+z_0)^{2\nu_2}} - 1 \right)^{3/2} F \left( \frac{3}{2}, 1 + \frac{1}{2\nu_2}; \frac{5}{2}; 1 - \frac{u^2}{a_2^2 (h+z_0)^{2\nu_2}} \right) \right]. \quad (7)$$

234 In the WKB approximation, the reflection coefficient from the turning point equals  
235  $V_2 = \exp(-i\pi/2)$ .<sup>23</sup> The reflection coefficient from the boundary  $z = 0$ , where  $c_s$  vanishes and the  
236 shear speed gradient becomes infinite, has been found in Refs. 9 and 17 and equals

237 
$$V_1 = \exp \left( \frac{-i\pi\nu_1}{2(1-\nu_1)} \right) \quad (8)$$

238 for *SH* waves. Using these reflection coefficients  $V_1$  and  $V_2$ , from the dispersion equation (3) we  
 239 find the frequency of the *SH* interface wave with a turning point in one of the sediment layers:

240 
$$f_n = \left[ \frac{n}{2} + \frac{4\nu_1 - 3}{8(1-\nu_1)} \right] \big/ \varphi(z_t). \quad (9)$$

241 Here  $n = 1, 2, \dots$  is the order of the interface wave. Higher-order interface waves (normal  
 242 modes) have higher frequencies at the same value of the phase velocity  $u$ . Dependence of the  
 243 interface wave frequency on the phase speed enters Eq. (9) via  $\varphi(z_t)$ . Higher-order modes have  
 244 higher frequencies at the same value of the phase velocity  $u$  and higher phase speeds at the same  
 245 value of frequency. Explicit expressions for the phase integral in Eq. (9) are given by Eqs. (4)  
 246 and (6) when the turning point is located in the upper or lower sediment layer, respectively.

247 When there are no turning points and  $a_2(H+z_0)^{\nu_2} \leq u < c_{bs}$ , the wave is reflected from  
 248 the boundary  $z = H$ . The plane wave reflection coefficient of *SH* waves<sup>23</sup> at this boundary is

249 
$$V_2 = \exp(-2i\Phi_{SH}), \quad \Phi_{SH} = \arctan \left[ \frac{\rho_b c_{sb}^2}{\rho_2 a_2^2 (H+z_0)^{2\nu_2}} \sqrt{\frac{1-c_{sb}^{-2}u^2}{a_2^{-2} (H+z_0)^{-2\nu_2} u^2 - 1}} \right]. \quad (10)$$

250 From the dispersion equation (3) we find

251 
$$f_n = \left[ \frac{n}{2} + \frac{5\nu_1 - 4}{8(1-\nu_1)} + \frac{\Phi_{SH}}{2\pi} \right] \big/ \varphi(H), \quad (11)$$

252 where the phase integral is given by Eq. (7). Finally, when  $a_1 h^{\nu_1} \leq u \leq a_2 (h+z_0)^{\nu_2}$ , reflection  
 253 occurs at  $z = h$ . The result is similar to Eq. (11) and differs by replacement of  $\varphi(H)$  with  $\varphi(h)$ , Eq.  
 254 (5). In addition, in the expression for the phase of the reflection coefficient in Eq. (10), one  
 255 should use elastic parameters in the vicinity of the boundary  $z = h$  and replace  $\rho_2$  with  $\rho_1, \rho_b$  with  
 256  $\rho_2, c_{sb}$  with  $a_2 (h+z_0)^{\nu_2}$ , and  $a_2 (H+z_0)^{\nu_2}$  with  $a_1 h^{\nu_1}$  (see Fig. 2).

257 In the special case, where  $a_1 = a_2$ ,  $v_1 = v_2$ ,  $z_0 = 0$ , and  $v_1 \rightarrow 0$  in Eqs. (1) and (2), we have a  
 258 homogeneous solid layer with the shear speed  $c_s = a_1$  that is located between homogeneous fluid  
 259 ( $z < 0$ ) and solid ( $z > H$ ) half-spaces. In this limit, our problem reduces to the textbook setting for  
 260 Love interface waves.<sup>35</sup> The resulting waveguide for *SH* waves is also equivalent to the acoustic  
 261 waveguide in a homogeneous fluid layer between a rigid boundary at  $z = 0$  and a homogeneous  
 262 fluid half-space  $z > H$ .<sup>23</sup> In the limit  $v_1 \rightarrow 0$ , Eq. (8) gives the correct result  $V_1 = 1$  for the  
 263 reflection coefficient of *SH* waves at the solid-fluid interface,<sup>23</sup> and Eq. (3) gives  
 264  $\varphi(H) = H\sqrt{a_1^{-2} - u^{-2}}$  for the phase integral. An inspection shows that the interface wave  
 265 frequencies  $f_n$ , that are predicted by Eq. (11) with  $v_1 = 0$ , agree with the textbook result<sup>35</sup> for the  
 266 Love wave dispersion in this special case.

267 Equations (4) and (9) show that frequency  $f_n$  of  $n$ -th interface wave is proportional to  
 268  $u^{1-1/v_1}$  when the turning point is located in the upper sediment layer. On the logarithmic scale, the  
 269 slope of the dispersion curve,  $d(\ln f_n)/d(\ln u) = 1 - v_1^{-1}$ , depends only on the shear-speed power-  
 270 law exponent in Eq. (1).

271 When the phase speed  $u$  is much larger than the shear speed around  $z = h$ , the turning  
 272 point is located deep in the lower sediment layer, and the vicinity of the turning point gives the  
 273 main contribution into the phase integral in Eq. (3). Indeed, it follows from Eqs. (5), (6), and the  
 274 equation<sup>34</sup>

$$275 \lim_{w \rightarrow \infty} \left[ (w^2 - 1)^{3/2} F\left(\frac{3}{2}, 1 + \frac{1}{2v}; \frac{5}{2}; 1 - w^2\right) \right] = \frac{3\sqrt{\pi} \Gamma((1-v)/2v)}{2\Gamma(1/2v)} \quad (12)$$

276 that under these conditions  $\varphi(z_t)$  is given approximately by Eq. (4) with  $a_1$  and  $v_1$  replaced with  
 277  $a_2$  and  $v_2$ , respectively. Then, the slope of the dispersion curves  $d(\ln f_n)/d(\ln u) = 1 - v_2^{-1}$  is  
 278 controlled by the shear-speed power-law exponent in Eq. (2).

279 The dispersion equations, which are derived for *SH* interface waves in this section and for  
 280 *P*–*SV* waves in Sec. 2B, describe a gradual transition between the limiting cases of the constant  
 281 slope of the dispersion curves.

282

283 **B. Dispersion relations of vertically polarized interface waves**

284 Unlike horizontally polarized (*SH*) shear waves, vertically polarized (*SV*) shear waves are  
 285 coupled to compressional (*P*) waves by the shear-speed gradients. In the case of the power-law  
 286 shear velocity profile, the coupling is particularly strong near the seafloor  $z = 0$ .<sup>17</sup> *P*–*SV* coupling  
 287 leads to appearance of two types of slow interface waves that are supported by soft marine  
 288 sediments, the fundamental mode and the main sequence modes.<sup>10, 17</sup> The main sequence modes  
 289 are uncoupled from the water column, just like *SH* interface waves. In the WKB approximation,  
 290 dispersion equation (3) of the main sequence modes differs from that for *SH* waves by having a  
 291 different reflection coefficient<sup>17</sup>  $V_1$  from the boundary  $z = 0$  [cf. Eq. (8)]:

292 
$$V_1 = \exp\left(\frac{i\pi(2-3\nu_1)}{2(1-\nu_1)}\right). \quad (13)$$

293 *SV* reflection coefficient at interfaces, where parameters of the solid are discontinuous, is also  
 294 different from the reflection coefficient Eq. (10) of *SH* waves. In particular, the *SV* reflection  
 295 coefficient from the boundary  $z = H$  can be written as  $V_2 = \exp(-2i\Phi_{SV})$ , where

296 
$$\Phi_{SV} = \arctan \left[ \frac{\sqrt{1-\frac{u^2}{C^2}} \left[ \frac{Mu^4}{4C^4} + \left( N^{-2} - M - \frac{u^2}{2C^2} \right)^2 \right] - \left[ N^{-2} - M + (M-1) \frac{u^2}{2C^2} \right]^2}{\sqrt{\frac{N^2 u^2}{C^2} - 1} \left[ \frac{Mv^4}{4C^4} + \left( N^{-2} - M + M \frac{u^2}{2C^2} \right)^2 - (N^{-2} - M)^2 \sqrt{1 - \frac{u^2}{C^2}} \right]} \right], \quad (14)$$

297  $C = c_{sb}$ ,  $M = \rho_b/\rho_2$ , and  $N = a_2^{-1} (H + z_0)^{-\nu_2} c_{sb}$ .  $C$ ,  $N$ , and  $M$  have the meaning of the shear speed  
 298 below the boundary, the ratio of the shear speeds just above and just below the boundary, and the  
 299 ratio of densities above and below the boundary, respectively. Equation (14) has been obtained  
 300 from the general equation for the plane wave reflection coefficient of  $SV$  waves at solid-solid  
 301 interface [see, e.g., Eq. (4.2.9) in Ref. 23] in the limit when  $c_s/c_l \rightarrow 0$  in both solids.

302 Solving the dispersion equation (3) for the main sequence modes with appropriate  
 303 reflection coefficients  $V_1$  and  $V_2$ , we obtain

$$304 f_n = \left[ \frac{n}{2} + \frac{2\nu_1 - 1}{8(1 - \nu_1)} \right] / \varphi(z_t) \quad (15)$$

305 for the waves with a turning point in one of the sediment layers. Here, as in Eq. (9) for  $SH$   
 306 modes, the phase integral is given by Eq. (4), when  $0 < u < a_1 h^{\nu_1}$ , and by Eq. (6), when  
 307  $a_2 (h + z_0)^{\nu_2} < u < a_2 (H + z_0)^{\nu_2}$ . When  $a_2 (H + z_0)^{\nu_2} \leq u < c_{bs}$ , waves are reflected from the  
 308 boundary  $z = H$ , and we find

$$309 f_n = \left[ \frac{n}{2} + \frac{3\nu_1 - 2}{8(1 - \nu_1)} + \frac{\Phi_{SV}}{2\pi} \right] / \varphi(H) \quad (16)$$

310 from Eqs. (3), (13), and (14). The phase integral in Eq. (16) is given by Eq. (7). Finally, when  
 311  $a_1 h^{\nu_1} \leq u \leq a_2 (h + z_0)^{\nu_2}$ , waves are reflected at  $z = h$ . The result in this case differs from Eq. (16)  
 312 by substitution of  $\varphi(h)$ , Eq. (5), for  $\varphi(H)$ . In addition,  $C = a_2 (h + z_0)^{\nu_2}$ ,  $M = \rho_2/\rho_1$ , and  
 313  $N = a_1^{-1} h^{-\nu_1} a_2 (h + z_0)^{\nu_2}$  in Eq. (14) for this boundary.

314 The accuracy of the WKB-based asymptotic dispersion equations increases with  
 315 increasing mode order,<sup>17</sup> and the results may not be reliable at  $n = 1$ . In addition, the WKB  
 316 approximation gives discontinuous results and is not accurate when turning points approach and

317 cross interfaces, where elastic parameters are discontinuous, i.e., in the vicinity of  $u=a_1 h^{\nu_1}$ ,

318  $u=a_2(h+z_0)^{\nu_2}$ , and  $u=a_2(H+z_0)^{\nu_2}$ .

319 An alternative approach to approximating the dispersion equation, which is particularly  
 320 useful for low-order modes, was developed in Ref. 17. The approach takes advantage of the  
 321 availability of an exact solution, when the power-law exponent  $\nu_1 = 0.5$ , and builds a perturbation  
 322 theory with respect to the parameter  $|\nu_1 - 0.5|$  that is assumed to be small compared to unity. In  
 323 marine sediments,  $|\nu_1 - 0.5| < 0.5$  and is often rather small. When the shear speed in soft sediments  
 324 follows the power law, by neglecting terms of second and higher order in  $|\nu_1 - 0.5|$ , the dispersion  
 325 equation of the main sequence of *P*–*SV* interface waves can be written as<sup>17</sup>

$$326 f_n = \frac{\Gamma(1/2\nu_1) a_1^{\nu_1} u^{1-\nu_1}}{2\sqrt{\pi} \Gamma((1-\nu_1)/2\nu_1)} \left[ 2n + (2\nu_1 - 1) \left( \frac{3-2\nu_1}{2-2\nu_1} + \frac{1}{n} + 2n\psi(n) - 2n\ln n \right) \right], \quad (17)$$

327 for arbitrary  $n = 1, 2, \dots$ . Under the same assumptions, the dispersion equation of the  
 328 fundamental mode is<sup>17</sup>

$$329 f_0 = \frac{(2a_1)^{\nu_1} u^{1-\nu_1}}{4\pi(1+\rho_1/\rho_w)^{\nu_1/2}} \exp \left[ \frac{2\nu_1 - 1}{2\nu_1} (1 - \gamma) \right]. \quad (18)$$

330 Here  $\gamma = 0.57721\dots$  is the Euler's constant, and  $\psi$  stands for Digamma function.<sup>34</sup> The  
 331 counterpart of Eq. (17) for *SH* waves is<sup>17</sup>

$$332 f_n = \frac{\Gamma(1/2\nu_1) a_1^{\nu_1} u^{1-\nu_1}}{2\sqrt{\pi} \Gamma((1-\nu_1)/2\nu_1)} \left\{ 2n - 1 + (2\nu_1 - 1)(2n - 1) \left[ \psi(n) - \ln \left( n - \frac{1}{2} \right) \right] + \frac{2\nu_1 - 1}{2 - 2\nu_1} \right\}. \quad (19)$$

333 As discussed in Ref. 17, Eqs. (17) (19) can be used for interface waves in the case of a  
 334 multi-layered seabed provided the turning point is located in the upper soft sediment layer with a  
 335 power-law shear speed profile. Equations (17) (19) complement the asymptotic dispersion

336 equations (9) and (15) for the low-order, low-speed modes, for which the WKB-based results are  
 337 either unavailable or not reliable.

338

339 **C. Inversion of the interface wave dispersion data**

340 We employ the analytical dispersion relations obtained in Secs. 3A and 3B as the forward model  
 341 to match the measured values (Sec. II) of phase speeds of horizontally and vertically polarized  
 342 interface waves. A nonlinear least-squares method is used to fit all the data for both wave types  
 343 simultaneously. Data from the fundamental  $P-SV$  mode and the lowest order ( $n = 1$ )  $SH$  mode  
 344 are fit to the dispersion curve for the one-layer model, i.e., Eqs. (18) and (19), respectively. Data  
 345 for the higher-order modes are fit to the asymptotic dispersion relations, Eqs. (9) and (15), for the  
 346 two-layer model. Simultaneously fitting the data for all interface waves to multiple theoretical  
 347 dispersion curves reduces the goodness of fit for any one dispersion curve, but it ensures  
 348 consistency between sediment parameters estimated across all the curves.

349 It is assumed in the inversion that  $z_0 = 0$  in Eq. (2) and that all modes have turning points  
 350 above the bottom  $z = H$  of the second sediment layer. Then, the geoacoustic model contains six  
 351 unknown parameters: depth  $h$  of the boundary between sediment layers, the density ratio  $\rho_w/\rho_1$ ,  
 352 and the power-law parameters  $a_1, v_1, a_2, v_2$  in Eqs. (1) and (2). Results of the inversion, including  
 353 95% confidence bounds of the estimated parameters, are shown in Table 1. The estimated value  
 354 of the density ratio  $\rho_w/\rho_1 = 0.537$  in Table 1 corresponds to the density  $\rho_1 = 1910 \text{ kg/m}^3$  in the top  
 355 5.6 m of the seabed.

356

357

358

359

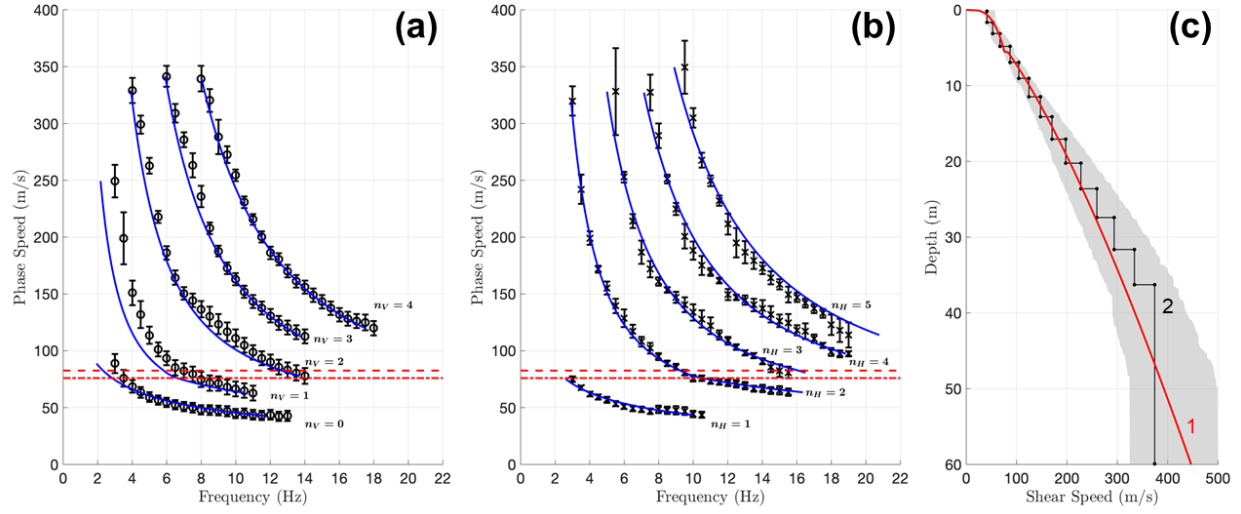
Table 1. Geoacoustic inversion parameters and results

Parameter	Unit	Estimated Value	95% Confidence Bounds
$\rho_w/\rho_1$	–	0.537	(0.479, 0.596)
$h$	m	5.57	(5.03, 6.11)
$a_1 (1m)^{v_1}$	m/s	46.3	(46.0, 46.7)
$v_1$	–	0.288	(0.277, 0.300)
$a_2 (1m)^{v_2}$	m/s	24.4	(22.5, 26.3)
$v_2$	–	0.710	(0.677, 0.742)

360

361 These parameters are used to generate a dispersion curve for each  $P$ – $SV$  and  $SH$  mode,  
 362 which are drawn as solid lines in Figs. 3a and 3b for comparison with the experimental data. A  
 363 dotted line marks the maximum phase speed with turning points in the first layer,  $u = a_1 h^{v_1}$ , and  
 364 a dashed line marks the minimum phase speed with turning points in the second layer,  $u = a_2 h^{v_2}$ .  
 365 All but one of the data points for the fundamental ( $n = 0$ )  $P$ – $SV$  and the first  $SH$  modes lie below  
 366 these lines, justifying the use of the single-layer model for them. The dispersion curve for the  
 367 mode  $n = 1$  in the main sequence of  $P$ – $SV$  modes is matched with larger errors than the other  
 368 modes ostensibly because the WKB approximation becomes more accurate as mode number  $n$   
 369 increases.

370



371 **Figure 3. (Color online)** Results of an inversion of measured dispersion curves of the interface  
 372 waves for depth dependence of the shear speed. (a) Comparison of the theoretical frequency  
 373 dependence of the interface wave phase speed in an optimum two-layer model (solid lines) with  
 374 measured phase speeds of  $P$ - $SV$  interface waves. Error bars of measurements<sup>22</sup> are shown. (b)  
 375 Same for measured phase speeds of  $SH$  interface waves. Mode orders  $n_H$  and  $n_V$  of, respectively,  
 376 horizontally and vertically polarized interface waves are shown in the figure. Dashed and dotted  
 377 lines show inverted values of the shear speed below and above the interface  $z = h$  between the  
 378 soft sediment layers. (c) Comparison of the results of the parsimonious two-layer inversion (1)  
 379 with an inversion in terms of a large number of homogeneous layers<sup>22</sup> (2). The shaded region is  
 380 the overlap of 95% confidence intervals of the shear speed profile as obtained in Ref. 22 from the  
 381 separate Bayesian inversions of the dispersion curves of the horizontally and vertically polarized  
 382 interface waves.  
 383  
 384  
 385 Line 1 in Fig. 3c shows the shear speed profile as a function of depth using the  
 386 parameters from Table 1 and Eqs. (1) and (2). Line 2 is the multi-layer model from Dong et al.<sup>22</sup>

387 As noted in that paper, a single power-law profile is not a good fit for the data. Our two-layer  
 388 model is a better fit for the data and is in reasonable agreement with the multi-layer inversion  
 389 result, as discussed in more detail in Sec. V. The maximum phase speed in the data set, 350 m/s,  
 390 produces the greatest turning depth, 42.5 m. These data cannot be used to estimate shear speeds  
 391 at depths greater than this.

392

#### 393 **IV. RESONANT REFLECTION OF COMPRESSIONAL WAVES**

394 In this section we investigate the hypothesis that the strong, narrow peaks in the observed power  
 395 spectra of vertical and radial components of particle velocity (Fig. 1a) result from the  
 396 propagation conditions of  $P$ - $SV$  waves at the site of the experiment. We offer a physical  
 397 interpretation of these observations as resulting from resonantly enhanced reflection from the  
 398 layered seabed, relate the resonance to the shear speed inversion results, and discuss the  
 399 geoacoustic information contained in the peak frequency  $f_p = 38$  Hz.

400 Seismo-acoustic resonances are often observed, when surficial marine sediments have  
 401 low shear speeds, but at much lower frequencies between about 0.3–7.5 Hz, see, e.g., Refs. 9, 31,  
 402 32. Those resonances arise due to reflection of shear waves and, unlike the results illustrated in  
 403 Fig. 1a, are characterized by a large ratio of horizontal-to-vertical particle velocity amplitudes  
 404 and do not exhibit a large difference between amplitudes of two orthogonal horizontal  
 405 components of the particle acceleration.<sup>9</sup> In the North Sea experiment discussed in this paper, the  
 406 peak occurs at the frequency that is considerably larger than the frequencies of observed surface  
 407 waves and is, therefore, likely to be caused by compressional waves. The travel time  $1/f$   
 408 corresponding to the peak frequency is smaller than acoustic travel time from the source on the

409 seafloor to the ocean surface. Thus, any interference phenomena or resonances responsible for  
 410 the observed peak should be explained in terms of the ocean bottom properties.

411 Geoacoustic inversion of the measured dispersion curves of interface waves (Sec. 3C)  
 412 reveals a boundary between sediment layers at  $h \approx 5.6$  m below the seafloor. Shear speeds just  
 413 above and just below the boundary are approximately 76 and 83 m/s, which are much smaller  
 414 than the compressional wave speeds  $c_l$  in the sediments. Surficial sediments at the experimental  
 415 site are described as soft Holocene clays.<sup>29, 30</sup> For such sediments,  $c_l$  is expected to be somewhat  
 416 less than the sound speed in water near the bottom,  $c_w$ , and increase with the depth below  
 417 seafloor.<sup>7, 18, 36</sup>

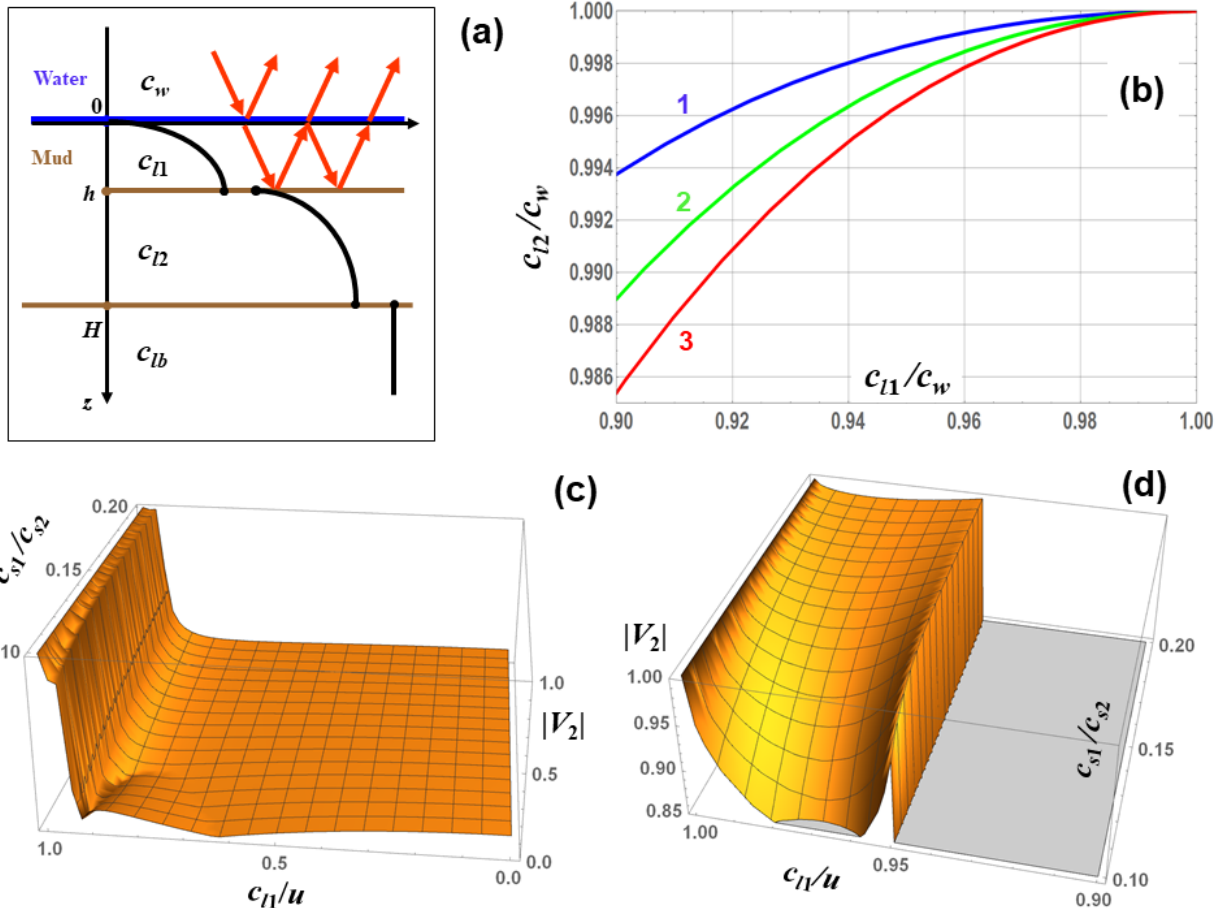
418 We will show that the power spectrum peak can be explained by the interference of  
 419 compressional waves reflected from the seafloor and the boundary  $z = h$  within sediments.  
 420 Consider first a simplified geoacoustic model, where shear rigidity is neglected at  $z < h$ , i.e., the  
 421 top layer of the bottom is approximated by a homogeneous fluid with sound speed  $c_{l1}$  (Fig. 4a).  
 422 The ocean bottom at  $z > h$  is modeled as a homogeneous solid half-space with compressional  
 423 wave speed  $c_{l2}$  and shear wave speed  $c_{s2}$ . The reflection coefficient of a plane acoustic wave  
 424 incident from water on the seafloor will be infinite when the following condition<sup>23</sup> is met:

$$425 \quad V_1 V_2 \exp\left(2i\omega h \sqrt{c_{l1}^{-2} - u^{-2}}\right) = 1. \quad (20)$$

426 Equation (20) is similar to Eq. (3) but refers to compressional waves, and reflection coefficients  
 427  $V_1$  and  $V_2$  have a different meaning. Here  $V_1$  and  $V_2$  are plane-wave reflection coefficients at  $z =$   
 428 0 and  $z = h$  for sound waves in the layer  $0 < z < h$ . As in Eq. (3),  $V_1$  and  $V_2$  are the reflection  
 429 coefficients for incidence from below and from above, respectively. In Eq. (20)  $u$  has the  
 430 meaning of the phase speed of the trace of sound waves on a horizontal plane; in terms of  $u$  and  
 431 wave frequency  $\omega$ , the horizontal component of the wave vector  $\xi = \omega/u$ . Equation (20) coincides

432 with the dispersion equation of acoustic normal modes with phase speed  $u$  in the waveguide  
 433 formed by the layer  $0 < z < h$ .

434



435

436 **Figure 4. (Color online)** Compressional wave resonance in a stratified seabed. (a) Geometry of  
 437 resonance reflection of compressional waves. Arrows illustrate incident, reflected, and  
 438 transmitted compressional waves. Constant compressional wave speeds in different layers are  
 439 indicated in the figure. A sketch of the depth dependence of the shear speed is shown for  
 440 orientation. (b) Relation between the compressional wave speeds in the upper ( $0 < z < h$ ) and  
 441 lower ( $h < z < H$ ) clay layers as derived from the observed resonance frequency for three values  
 442 of the ratio  $\rho_w/\rho_1$  of densities of the water and of the upper clay layer: 0.537 (1), 0.75 (2), and 0.9

443 (3). (c) Absolute value of the reflection coefficient  $V_2$  of plane compressional waves from  
 444 interface  $z = h$  of two solids with compressional speeds  $c_{l1} < c_{l2}$  and shear speeds  $c_{s1} < c_{s2}$ . The  
 445 wave is incident from the solid with the smaller wave speed. In the figure,  $c_{l1}/c_{l2} = 0.95$ ,  $c_{l1}/c_{s1} =$   
 446 20, and the ratio of densities of the two solids  $\rho_2/\rho_1 = 1.2$ . The angle of incidence  $\theta_l$  is related to  
 447 the trace velocity  $u$  of the wave by the equation  $\sin \theta_l = c_{l1}/u$ . (d) An expanded view of the part of  
 448 figure (c) at  $|V_2| > 0.85$  and  $0.9 < c_{l1}/u < 1$ .

449

450 For propagating (as opposed to evanescent) plane waves in the layer, the absolute values  
 451 of reflection coefficients  $V_1$  and  $V_2$  do not exceed unity. For the condition (20) to be met,  $|V_1|$  and  
 452  $|V_2|$  should be equal to 1 simultaneously. The reflection coefficient of a plane sound wave in fluid  
 453 from a solid half-space is<sup>23</sup>

$$454 V_2 = \frac{Z_l \cos^2 2\theta_s + Z_s \sin^2 2\theta_s - Z}{Z_l \cos^2 2\theta_s + Z_s \sin^2 2\theta_s + Z}. \quad (21)$$

455 Here  $Z_s$  and  $Z_l$  are impedances of shear and compressional waves at  $z > h$ ;  $Z$  is the impedance of  
 456 compressional waves at  $0 < z < h$ ; and  $\theta_s$  is the angle that wave vector of the shear wave, below  
 457 the interface, makes with the normal to the interface  $z = h$ :

$$458 \theta_s = \arcsin \frac{c_{s2}}{u}, \quad Z_s = \frac{\rho_2 c_{s2}}{\cos \theta_s}, \quad Z_l = \frac{\rho_2 c_{l2}}{\sqrt{1 - c_{l2}^2/u^2}}, \quad Z = \frac{\rho_1 c_{l1}}{\sqrt{1 - c_{l1}^2/u^2}}. \quad (22)$$

459 For a propagating compressional wave incident on a solid half-space with a shear speed smaller  
 460 than compressional speed  $c_{l1}$ ,  $\theta_s$  and impedances  $Z$  and  $Z_s$  are real and positive according to Eq.  
 461 (22). Then, it follows from Eq. (21) that  $|V_2| < 1$  unless  $u = c_{l2}$ . When  $u = c_{l2}$ , impedance  $Z_l$  is  
 462 infinite, and  $V_2 = 1$ . This property of the reflection coefficient has a simple physical meaning.  
 463 Acoustic waves cannot be totally reflected from the solid half-space because a part of the  
 464 incident energy is carried away from the boundary by shear waves in the solid. The only

465 exception occurs when the impedance of the refracted compressional wave in the solid becomes  
 466 infinite at  $u = c_{l2}$ , and the amplitude of the shear wave vanishes.<sup>23</sup>

467 The condition  $|V_1| = 1$  will be satisfied at  $u = c_{l2}$  provided

468  $c_{l1} < c_{l2} < c_w$ . (23)

469 This inequality ensures that the plane wave is totally reflected at the fluid-fluid interface  $z = 0$ .

470 The reflection coefficient from the top boundary of the layer, for incidence from below, is

471 
$$V_1 = \exp \left[ -2i \arctan \left( \frac{\rho_1}{\rho_w} \sqrt{\frac{1-u^2 c_w^{-2}}{u^2 c_{l1}^{-2} - 1}} \right) \right] \quad (24)$$

472 at total internal reflection.<sup>23</sup> Hence, the resonance condition (20) will be met at frequencies  $f_{l,j}$   
 473 that satisfy the following equation:

474 
$$\frac{2f_{l,j}h}{c_{l2}} \sqrt{\frac{c_{l2}^2}{c_{l1}^2} - 1} - \frac{1}{\pi} \arctan \left( \frac{\rho_1}{\rho_w} \sqrt{\frac{1-c_{l2}^2 c_w^{-2}}{c_{l2}^2 c_{l1}^{-2} - 1}} \right) = j, \quad j = 0, 1, 2, \dots \quad (25)$$

475 The above derivation of the resonance conditions (23) and (25) extends an earlier  
 476 discussion by Duncan et al.<sup>37</sup> of frequencies with sharply reduced transmission losses in an  
 477 underwater waveguide with a homogeneous solid bottom, when the sound speed in water is  
 478 larger than the shear wave speed and smaller than the compressional wave speed in the bottom.  
 479 The fluid-fluid boundary at  $z = 0$  in our problem reduces to a pressure release boundary in the  
 480 limit  $\rho_w \rightarrow 0$ . In this limiting case, the arctangent in Eq. (25) is replaced with  $\pi/2$ , and our result  
 481 reduces to that of Ref. 37. When  $\rho_w \rightarrow 0$ ,  $|V_1| = 1$  at all incidence angles and for any  $c_w$ , and the  
 482 requirement  $c_{l2} < c_w$  in Eq. (23) does not apply.

483 The lowest-frequency compressional wave resonance corresponds to  $j = 0$  in Eq. (25) and  
 484 occurs at the frequency

485 
$$f_{l,0} = \frac{c_{l2}}{2\pi h \sqrt{c_{l2}^2 c_{l1}^{-2} - 1}} \arctan \left( \frac{\rho_1}{\rho_w} \sqrt{\frac{1 - c_{l2}^2 c_w^{-2}}{c_{l2}^2 c_{l1}^{-2} - 1}} \right). \quad (26)$$

486 Subsequent resonances are equally spaced in frequency with the spacing

487 
$$f_{l,j+1} - f_{l,j} = \frac{c_{l2}}{2h \sqrt{c_{l2}^2 c_{l1}^{-2} - 1}}. \quad (27)$$

488 Note that the frequency difference  $f_{l,j+1} - f_{l,j} > c_{l1}/2h$ . Under the conditions of the North Sea  
 489 experiment, where  $h \approx 5.6$  m, the frequency spacing exceeds 85 Hz for all reasonable values of  
 490  $c_{l1} > 1000$  m/s, and – in agreement with the observations<sup>22</sup> – only one resonance,  $f_{l,0}$ , is observed  
 491 within the 2–60 Hz frequency band of the source.

492 With the resonance frequency  $f_{l,0}$ , layer thickness  $h$ , and sound speed in water known, Eq.  
 493 (26) relates three geoacoustic parameters: compressional wave speeds  $c_{l1}$  and  $c_{l2}$  in two sediment  
 494 layers and the ratio  $\rho_w/\rho_1$  of water and sediment layer densities (Fig. 4b). The value  $\rho_w/\rho_1 =$   
 495 0.537 has been obtained from the interface wave data (Table 1). If  $c_{l2}$  were retrieved from, say,  
 496 measured travel times of compressional head wave data,<sup>38,39</sup>  $c_{l1}$  could be unambiguously  
 497 determined from Eq. (26), and vice versa. In the North Sea experiment, the nondimensional  
 498 parameter  $f_{l,0} h/c_w \approx 0.14$  is small. Then, Eq. (26) provides a strong constraint on deviations of  
 499 the ratios  $c_{l1}/c_w$  and especially  $c_{l2}/c_w$  from unity (Fig. 4b). The findings that  $c_{l1}$  and  $c_{l2}$  are  
 500 smaller than but close to the sound speed in water are consistent with the available geologic  
 501 information about surficial sediments<sup>30</sup> and expectations for compressional wave speeds in soft  
 502 clays.<sup>7, 18, 36</sup>

503 In the above discussion we modeled the top sediment layer  $0 < z < h$  as a fluid. To justify  
 504 the application of the fluid-solid model to the interface  $z = h$  between sediment layers, it should  
 505 be noted first that the layer thickness  $h = 5.57$  m is small compared to the compressional wave  
 506 wavelength  $c_{l1}/f_p \sim 40$  m. For compressional waves, the upper layer will act as a homogeneous

507 layer with some effective (averaged) parameters. Given the very fast relative variations of the  
 508 shear rigidity with depth and that shear rigidity is extremely small in the upper part of the layer,  
 509 the effective shear speed will be much smaller than the 73 m/s shear speed just above the  
 510 boundary  $z = h$ . Similarly, the shear modulus increases by the factor of  $\sim 20$  over the first 40 m  
 511 below the boundary (see Table 1). In a homogeneous half-space model of the sediments at  $z > h$ ,  
 512 the effective shear speed should be considerably larger than the 85 m/s value just below the  
 513 interface as given by the geoacoustic inversion of the interface wave data. Hence, reflection of  
 514 compressional waves from the boundary  $z = h$  should be treated as reflection at a solid-solid  
 515 interface with a large contrast in shear speeds.

516 Figure 4c illustrates the angular dependence of the reflection coefficient  $V_2$  of a plane  
 517 compressional wave from the interface of two homogeneous solids with a large contrast between  
 518 shear speeds ( $c_{s2} \gg c_{s1}$ ). The wave is incident from the solid with a smaller shear and  
 519 compressional speeds ( $c_{l2} > c_{l1}$ ). Incidence angle  $\theta_l$  of the wave is related to the trace velocity  $u$   
 520 by the equation  $\sin\theta_l = c_{l1}/u$ . The reflection coefficient is calculated using Eqs. (4.2.8), (4.2.13)–  
 521 (4.2.13) in Ref. 23. The equations are exact but cumbersome and will not be reproduced here.  $V_2$   
 522 is real-valued at  $0 \leq u \leq c_{l2}$  and positive at  $u = c_{l2}$ . Note that  $|V_2|$  is relatively small at steep and  
 523 moderate incidence angles and, just like reflection coefficient Eq. (21) from a fluid-solid  
 524 interface, has a sharp maximum at  $u = c_{l2}$  (Figs. 4c, d). The value of  $|V_2(u = c_{l2})|$  is close to unity,  
 525 and the sharp local maximum of  $|V_2|$  leads to resonance reflection of compressional waves from  
 526 the layer  $0 < z < h$  at the frequencies satisfying Eq. (25) as in the case of reflection from a fluid  
 527 layer between fluid and solid half-spaces. In this model, the sharpness of the observed resonance  
 528 peaks (see Fig. 1a) is related to the sharpness of the angular dependence of the reflection  
 529 coefficient around its local maximum at  $u = c_{l2}$  in Fig. 4d.

530 When the layer  $0 < z < h$  has small but finite shear rigidity, the reflection coefficient  $V_1$   
 531 from the upper boundary  $z = 0$  of the layer deviates from the reflection coefficient Eq. (24) at a  
 532 fluid-fluid interface. The reflection coefficient of compressional waves in a solid at the solid-  
 533 fluid interface is

$$534 V_1 = \frac{Z - Z_l \cos^2 2\theta_s + Z_s \sin^2 2\theta_s}{Z + Z_l \cos^2 2\theta_s + Z_s \sin^2 2\theta_s}, \quad (28)$$

535 see, e.g., Eq. (4.2.37) in Ref. 23. The reflection coefficient is similar to that of the plane wave  
 536 incident on the interface from the fluid side, Eq. (21). At boundary  $z = 0$ ,

$$537 \theta_s = \arcsin \frac{c_{s1}}{u}, \quad Z_s = \frac{\rho_1 c_{s1}}{\cos \theta_s}, \quad Z_l = \frac{\rho_1 c_{l1}}{\sqrt{1 - c_{l1}^2/u^2}}, \quad Z = \frac{\rho_w c_w}{\sqrt{1 - c_w^2/u^2}} \quad (29)$$

538 in Eq. (28). When shear speed  $c_{s1}$  is small,  $\theta_s$  and  $Z_s$  are proportional to the small parameter  $c_{s1}/u$   
 539  $\ll 1$ . When  $c_{l1} \leq u \leq c_w$ ,  $Z$  is purely imaginary, and it follows from Eq. (28) that  $|V_1| = 1$  up to  
 540 terms of the third order in  $c_{s1}/u$ ; phase of the reflection coefficient differs from its value in Eq.  
 541 (24) [i.e., at  $c_{s1} = 0$ ] by terms  $O((c_{s1}/u)^2)$ . Thus, deviations of  $V_1$  from Eq. (24) are negligible.

542 Together with the above analysis of  $V_2$  (Figs. 4c, d), these findings justify application of  
 543 the resonance conditions Eqs. (23) and (25) in our problem.

544

## 545 V. DISCUSSION

546 Identification of the fundamental mode of  $P$ - $SV$  interface waves as the only mode that is  
 547 sensitive to sediment density has allowed us to retrieve an estimate  $\rho_w/\rho_1 = 0.537$  of the density  
 548 contrast between water and the sediment layer  $0 < z < h$ . In previous geoacoustic inversions<sup>22, 30</sup>  
 549 of the same data set, density was not retrieved. In the two density models postulated in Ref. 30  
 550 on the basis of the available geologic information at the experimental site, the density ratio  $\rho_w/\rho_1$   
 551 = 0.574–0.583, if the average of density in the upper 6 m of the sediments is taken for  $\rho_1$ . These

552 values are close to the value retrieved in Sec. 2C and are within the uncertainty interval of that  
 553 estimate, see Table 1.

554       Similarly, depth-independent compressional wave speed  $c_l = c_w$  in the seabed was  
 555 postulated in Ref. 30. In Ref. 22, interface wave dispersion curves were found to be insensitive to  
 556 the compressional speed, which was also assumed to be depth-independent. The relatively small  
 557 deviations of  $c_{l1}$  and  $c_{l2}$  from  $c_w$  that are derived in Sec. IV from the measured frequency of the  
 558 compressional wave resonance, are consistent with the rough depth-independent models.<sup>22,30</sup>  
 559 Furthermore, the power spectrum data provides strong constraints on variations of the  
 560 compressional wave speed across the seafloor and within top sediment layers (Fig. 4b).

561       Inversion of the interface wave dispersion data is accomplished in Sec. 2C by  
 562 representing the upper 40–50 m of the seabed by two layers with power-law profiles of the shear  
 563 speed. The model is motivated by the observation of two distinct slopes in log-log representation  
 564 of the dispersion curves (Fig. 1b). To assess this shear-speed model, it is compared here to  
 565 several alternative geoacoustic models of soft marine sediments. We have considered three  
 566 additional models of the shear speed depth dependence: single power-law layer, three power-law  
 567 layers, and two power-law layers on top of a homogeneous half-space. In the last two models,  
 568  $c_s(z) = a_2 z^{\nu_2}$  at  $h < z < H$ . Below the bottom of the second layer, at  $z > H$ ,  $c_s(z) = a_3 z^{\nu_3}$  in the  
 569 three-layer model; in the two-layer plus half-space model, the shear speed and density in the  
 570 half-space are  $c_{sb} = N a_2 H^{\nu_2}$  and  $\rho_b = M \rho_2$ . Parameters  $M$  and  $N$  have the same meaning as in Eq.  
 571 (14).

572       In the single-layer model, we have used the more accurate theoretical dispersion  
 573 equations (17)–(19) for all modes. In conjunction with the other models, Eqs. (18) and (19) have  
 574 been used for the fundamental ( $n = 0$ )  $P$ – $SV$  mode and  $SH$  mode 1, implying that those modes

575 interact only with the uppermost layer; the WKB approximation has been used for all other  
 576 modes. The  $P$ - $SV$  mode 1 data is not well-described by the WKB approximation and therefore  
 577 does not have a good fit for any model. It might have been useful to exclude that data from the  
 578 fit, but that has not been attempted.

579         Results of the interface wave data inversion in the alternative geoacoustic models are  
 580 summarized in Table 2 and illustrated in Fig. 5. Ninety-five per cent confidence bounds are  
 581 given in Table 2 for parameters of the retrieved power-law dependencies. The two-layer model  
 582 (Figs. 3a, b) shows major improvement over the one-layer model (Figs. 5a, b) in fitting the data.  
 583 This is reflected in the  $R^2$  values for the inversions, which increase from 0.966 for the one-layer  
 584 model to 0.980 for the two-layer model. The difference in the  $R^2$  values represents a decrease of  
 585 the model-data misfit variance by the factor of 1.7 in the two-layer model. Comparison of Figs.  
 586 5a, b and 3a, b demonstrates that the one-layer model fails to fit the data at phase speeds below  
 587 75–80 m/s. The data-model mismatch is so big (Figs. 5a, b) that  $R^2$  values calculated for the  
 588 fundamental  $P$ - $SV$  mode, −1.10, and the first  $SH$  mode, −3.07, prove to be negative. In contrast,  
 589 the two-layer model adequately approximates the low-order mode data, with  $R^2$  of 0.966 and  
 590 0.926 for the fundamental  $P$ - $SV$  mode and the first  $SH$  mode, respectively.

591         The physics behind the difficulties that the one-layer model has with low-order modes  
 592 can be traced back to the fact that dispersion of slow interface wave is most sensitive to the shear  
 593 speeds at depths around the turning point (Sec. 3A). Parameters of the optimum one-layer model  
 594 are primarily controlled by properties of the second layer ( $z > h$ ), where turning points are  
 595 located for most modes in the dataset. At phase speeds below 76 m/s, the turning points are  
 596 located in the top layer,  $0 < z < h$ , and the mismatch between the data and one-layer model  
 597 reflects the difference between the parameters of the two sediment layers.

598        The two-layer plus half-space model had the same  $R^2$  and produced identical estimated  
 599        values of parameters of the layers and extremely close confidence intervals of theses parameters  
 600        (Table 2) as the two-layer model (Table 1), suggesting that the data does not contain the wave  
 601        frequencies and mode orders that interacted with seabed below the bottom of the second power-  
 602        law layer. Despite an increase in the number of degrees of freedom, the three-layer model does  
 603        not noticeably improve the dispersion data fit ( $R^2 = 0.981$ ) and shows very low sensitivity to  
 604        parameters of the deepest layer, as reflected in the confidence intervals for  $H$ ,  $v_3$ , and especially  
 605         $a_3$ . We conclude that the two-layer model is in the best agreement with available dispersion data.

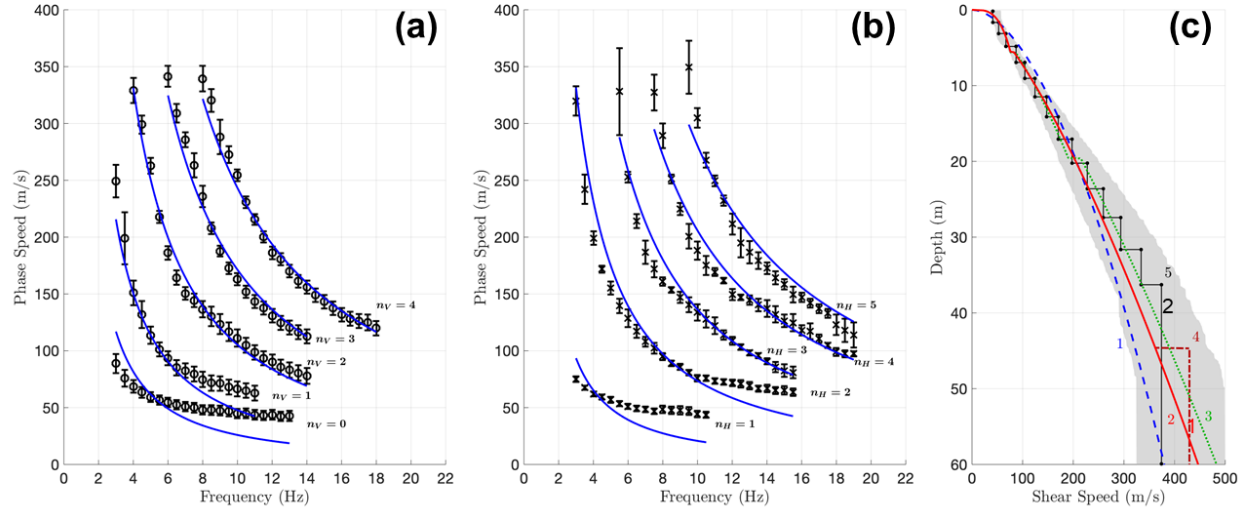
606        We have also considered a more general two-layer model, where non-zero values of the  
 607        parameter  $z_0$  in Eq. (2) are allowed, and  $z_0$  is considered as an additional unknown geoacoustic  
 608        parameter. Despite an increase in the number of degrees of freedom, no noticeable improvement  
 609        in the model-data fit was found compared to the original two-layer geoacoustic model in Table 1.

610        A Bayesian multi-layer shear-speed inversion of the interface wave dispersion data was  
 611        developed by Dong et al.<sup>22</sup> and considered as an approximation to the linear shear speed profile  
 612        in a layer overlying a homogeneous half-space. The multi-layer model<sup>22</sup> ensures an excellent fit  
 613        to the measured dispersion curves but its interpretation as an approximation to a linear profile is  
 614        questionable. Sediments with linear ( $v_1 = 1$ ) profile, unlike power-law profiles with  $0 < v_1 < 1$ ,  
 615        support neither  $SH$  nor slow  $P-SV$  interface waves.<sup>9, 17</sup> This can be traced back to the fact that,  
 616        when  $v_1 \geq 1$ , shear speed decreases so fast near  $z = 0$  that shear wave travel time to the seafloor  
 617        becomes infinite, the waves experience extraordinary attenuation and never reach the seafloor.

618  
 619

Table 2. Alternative geoacoustic models

Parameter	Unit	Single power-law layer			Two power-law layers overlying half-space			Three power-law layers		
		Estimated value	95% Confidence Bounds	Estimated value	95% Confidence Bounds	Estimated value	95% Confidence Bounds	Estimated value	95% Confidence Bounds	Estimated value
$\rho_w/\rho_1$	—	0.624	(0.446, 0.795)	0.537	(0.478, 0.596)	0.535	(0.475, 0.593)			
$h$	m	—	—	5.57	(5.02, 6.11)	5.68	(5.25, 6.11)			
$a_1 (1\text{m})^{v_1}$	m/s	39.0	(38.46, 39.58)	46.3	(46.0, 46.7)	46.3	(46.0, 46.7)			
$v_1$	—	0.556	(0.5475, 0.564)	0.288	(0.276, 0.301)	0.288	(0.277, 0.300)			
$a_2 (1\text{m})^{v_2}$	m/s	—	—	24.4	(22.5, 26.3)	28.9	(22.5, 26.3)			
$v_2$	—	—	—	0.710	(0.677, 0.743)	0.634	(0.580, 0.688)			
$H$	m	—	—	44.68	—	19.6	(15.75, 23.4)			
$M$	—	—	—	2.56	—	—	—			
$N$	—	—	—	1.185	—	—	—			
$a_3 (1\text{m})^{v_3}$	m/s	—	—	—	—	24.9	(-16.0, 65.8)			
$v_3$	—	—	—	—	—	0.710	(0.677, 0.742)			



621

622 **Figure 5. (Color online)** Inversion of measured dispersion curves of the interface waves for the  
 623 shear-speed profile in alternative geoacoustic models. (a) Comparison of the theoretical  
 624 frequency dependence of the phase speeds of interface waves in the optimum single-layer model  
 625 (solid lines) with measured phase speeds of  $P$ - $SV$  interface waves. Error bars of measurements<sup>22</sup>  
 626 are shown. (b) Same for measured phase speeds of  $SH$  interface waves. Mode orders  $n_H$  and  $n_V$   
 627 of, respectively, horizontally and vertically polarized interface waves are shown in the figure.  
 628 Note much poorer data-model agreement than in the two-layer inversion illustrated in Figs. 3a, b.  
 629 (c) Comparison of the results of alternative single-layer (1), two-layer (2), three-layer (3), and  
 630 two-layer plus half-space (4) power-law inversions with an inversion in terms of a large number  
 631 of homogeneous layers<sup>22</sup> (5). The shaded region is the overlap of 95% confidence intervals of the  
 632 shear speed profile as obtained in Ref. 22 from the separate Bayesian inversions of the dispersion  
 633 curves of the horizontally and vertically polarized interface waves.

634

635 The results of the multi-layer shear-speed inversion<sup>22</sup> are compared to results of various  
 636 simple, power-law based inversions in Figs. 3c and 5c. (Inversion results are extended to the 60

637 m depth below the seafloor, as in Ref. 22, although these may be only supported by data up to  
 638 about 45 m depth.) The results of power-law inversions, except the single-layer inversion, do not  
 639 deviate far from the multi-layer geoacoustic model in the top 50 m of the seabed. The two-layer,  
 640 two-layer plus half-space, and three-layer models are all well within the 95% confidence  
 641 intervals<sup>22</sup> of the Bayesian multi-layer inversions for *SH* and *P–SV* waves. Thus, the three simple  
 642 models and particularly the physics-guided, parsimonious two-layer inversion provide a shear-  
 643 speed depth dependence, which is arguably as consistent with the data as the much more  
 644 sophisticated and computationally intensive multi-parameter, multi-layer Bayesian inversion.

645

## 646 VI. CONCLUSION

647 Soft surficial sediments support a rich set of slow interface waves, which can account for the  
 648 bulk of seismo-acoustic energy near the seafloor at low frequencies (between about 1 Hz and a  
 649 few tens of Hertz) and are sensitive to the magnitude and depth-dependence of shear rigidity.  
 650 Hydrophone measurements miss most of the interface waves. Vector sensors, such as tri-axial,  
 651 bottom coupled accelerometers, are necessary to capture, separate different polarizations, and  
 652 identify various interface wave modes and other components of the full wave field.

653 The linear dependence between logarithms of the phase (or group) speeds of the interface  
 654 waves and their frequency was proposed by Chapman and Godin<sup>10, 17</sup> as means to identify a  
 655 seabed with a power-law shear-speed profile and determine its parameters. In this paper, that  
 656 simple, physics-based approach to geoacoustic inversions is extended to seabeds containing  
 657 several layers of soft sediments of different composition. In application to interface wave  
 658 dispersion data obtained in the North Sea off Norway, the approach leads to a low-parameter  
 659 model of the shear speed profile as power-law dependences in two layers. The model provides a

660 good fit to the data and agrees with the results of a much more elaborate Bayesian inversion.<sup>22</sup> In  
661 addition, a boundary between soft sediment layers is detected and sediment density is evaluated,  
662 with the result being consistent with available geologic information.

663 We identified a physical mechanism, which can lead to compressional wave resonances  
664 in stratified soft sediments, and demonstrated that the proposed mechanism can explain sharp  
665 peaks of the observed power spectra of the vertical and radial components of the particle  
666 velocity. The compressional wave resonance with a high quality factor is made possible by the  
667 fact that amplitudes of converted shear waves, which would otherwise take energy from and  
668 attenuate the compressional wave at reflection from a fluid-solid or solid-solid interface, are  
669 strongly suppressed at a particular incidence angle.

670 A simple, physics-guided approach presented in this paper results in a geoacoustic model  
671 that offers a consistent interpretation and a quantitative description of various salient features of  
672 the available data of the 2007 shear-wave experiment in the North Sea.

673

#### 674 **ACKNOWLEDGMENTS**

675 Statoil acquired and provided the data used in this research. This work was supported in part by  
676 the Office of Naval Research, awards N00014-17WX00773 and N00014-20WX01312. Helpful  
677 discussions with S. E. Dosso, N. R. Chapman, and A. D. Pierce are gratefully acknowledged.

678

679 **References**

- 680 <sup>1</sup> F. Gassmann, "Elastic waves through a packing of spheres," *Geophysics* **16**, 673–685 (1951).
- 681 <sup>2</sup> J. D. Goddard, "Nonlinear elasticity and pressure-dependent wave speeds in granular media,"
- 682 *Proc. R. Soc. London. Ser. A: Math. Phys. Sci.* **430**(1878), 105–131 (1990).
- 683 <sup>3</sup> S. N. Domenico, "Elastic properties of unconsolidated porous sand reservoirs," *Geophysics*,
- 684 **42**(7), 1339–1368 (1977).
- 685 <sup>4</sup> E. I. Hamilton, "Attenuation of shear waves in marine sediments," *J. Acoust. Soc. Am.* **60**,
- 686 334–338 (1976).
- 687 <sup>5</sup> G. M. Bryan and R. D. Stoll, "The dynamic shear modulus of marine sediments," *J. Acoust.*
- 688 *Soc. Am.* **83**, 2159–2164 (1988).
- 689 <sup>6</sup> M. D. Richardson, E. Muzi, B. Miaschi, and F. Turgutcan, "Shear wave velocity gradients in
- 690 near-surface marine sediments," in *Shear Waves in Marine Sediments*, edited by J. M. Hovem,
- 691 M. D. Richardson, and R. D. Stoll (Kluwer, Dordrecht, 1991), pp. 295–304.
- 692 <sup>7</sup> J. C. Osler and D. M. F. Chapman, "Seismo-acoustic determination of the shear-wave speed of
- 693 surficial clay and silt sediments on the Scotian shelf," *Canadian Acoustics*, **24**(4), 11–22 (1996).
- 694 <sup>8</sup> F. A. Bowles, "Observations on attenuation and shear-wave velocity in fine-grained, marine
- 695 sediments," *J. Acoust. Soc. Am.* **101**, 3385–3397 (1997).
- 696 <sup>9</sup> O. A. Godin and D. M. F. Chapman, "Shear speed gradients and ocean seismo-acoustic noise
- 697 resonances," *J. Acoust. Soc. Am.* **106**(5), 2367–2382 (1999).
- 698 <sup>10</sup> D. M. F. Chapman and O. A. Godin Dispersion of interface waves in sediments with power-
- 699 law shear speed profiles. II: Experimental observations and seismo-acoustic inversions, *J.*
- 700 *Acoust. Soc. Am.* **110**, 1908–1916 (2001).

- 701 <sup>11</sup> K. Ohta, S. Matsumoto, K. Okabe, K. Asano, and Y. Kanamori, "Estimation of shear wave  
702 speed in ocean-bottom sediment using electromagnetic induction source," *IEEE J. Ocean. Eng.*  
703 **33**(3), 233–239 (2008). doi: 10.1109/JOE.2008.926108.
- 704 <sup>12</sup> J. Dettmer, S. E. Dosso, and J. C. Osler, "Bayesian evidence computation for model selection  
705 in non-linear geoacoustic inference problems," *J. Acoust. Soc. Am.* **128**, 3406–3415 (2010).  
706 <https://doi.org/10.1121/1.3506345>
- 707 <sup>13</sup> H. Dong and S. E. Dosso, "Bayesian inversion of interface-wave dispersion for seabed shear-  
708 wave speed profiles," *IEEE J. Oceanic Eng.* **36** (1), 1–11 (2011).  
709 <https://doi.org/10.1109/JOE.2010.2100490>
- 710 <sup>14</sup> M. M. Haney and V. C. Tsai, "Nonperturbational surface-wave inversion: A Dix-type relation  
711 for surface waves," *Geophysics* **80** (6), EN167–EN177 (2015).
- 712 <sup>15</sup> A. G. Soloway, P. H. Dahl, and R. I. Odom, "Modeling explosion generated Scholte waves in  
713 sandy sediments with power law dependent shear wave speed," *J. Acoust. Soc. Am.* **138**,  
714 EL370–EL374 (2015). <https://doi.org/10.1121/1.4931831>
- 715 <sup>16</sup> E. Cunningham and V. Lekic, "Constraining properties of sedimentary strata using receiver  
716 functions: An example from the Atlantic Coastal Plain of the southeastern United States," *Bull.  
717 Seismol. Soc. Am.* **110**, 519–533 (2020). doi: 10.1785/0120190191
- 718 <sup>17</sup> O. A. Godin and D. M. F. Chapman, "Dispersion of interface waves in sediments with power-  
719 law shear speed profiles. I: Exact and approximate analytical results," *J. Acoust. Soc. Am.* **110**,  
720 1890–1907 (2001).
- 721 <sup>18</sup> D. Jackson and M. Richardson, *High-Frequency Seafloor Acoustics* (Springer, New York,  
722 2007).

- 723 <sup>19</sup> D. Rauch, "Experimental and theoretical studies of seismic interface waves in coastal waters,"  
724 in *Bottom-Interacting Ocean Acoustics*, edited by W. A. Kuperman and F. B. Jensen (Plenum,  
725 New York, 1980), pp. 307–327.
- 726 <sup>20</sup> J. Ewing, J. A. Carter, G. H. Sutton, and N. Barstow, "Shallow water sediment properties  
727 derived from high-frequency shear and interface waves," *J. Geophys. Res.: Solid Earth*, **97**(B4),  
728 4739–4762 (1992).
- 729 <sup>21</sup> G. Nolet and L. M. Dorman, "Waveform analysis of Scholte modes in ocean sediment layers,"  
730 *Geophys. J. Int.* **125**(2), 385–396 (1996).
- 731 <sup>22</sup> H. Dong, T.-D. Nguyen, and K. Duffaut, "Estimation of seabed shear-wave velocity profiles  
732 using shear-wave source data," *J. Acoust. Soc. Am.* **134**, 176–184 (2013).
- 733 <sup>23</sup> L. M. Brekhovskikh and O. A. Godin, *Acoustics of Layered Media. 1: Plane and Quasi-Plane  
734 Waves*. 2nd edn. (Springer, Berlin etc., 1998), pp. 14–29, 87–98, 183–186, 218–226.
- 735 <sup>24</sup> A. Caiti, T. Akal, and R. D. Stoll, "Estimation of shear wave velocity in shallow marine  
736 sediments," *IEEE J. Ocean. Eng.* **19**, 58–72 (1994).
- 737 <sup>25</sup> S. A. Frivik, R. Allnor, and J. M. Hovem, "Estimation of shear wave properties in the upper  
738 seabed using seismo-acoustical interface waves," in *High Frequency Acoustics in Shallow  
739 Water*, edited by N. G. Pace, E. Pouliquen, O. Bergem, and A. P. Lyons (SACLANTCEN, La  
740 Spezia, Italy, 1997), pp. 155–162.
- 741 <sup>26</sup> S. E. Crocker, J. H. Miller, G. R. Potty, J. C. Osler, and P. C. Hines, "Nonlinear inversion of  
742 acoustic scalar and vector field transfer functions," *IEEE J. Ocean. Eng.* **37**(4), 589–606 (2012).  
743 doi: 10.1109/JOE.2012.2206852.

- 744 <sup>27</sup> J. Shi, S. E. Dosso, D. Sun, and Q. Liu, “Geoacoustic inversion of the acoustic-pressure  
 745 vertical phase gradient from a single vector sensor,” *J. Acoust. Soc. Am.* **146**(5), 3159–3173  
 746 (2019).
- 747 <sup>28</sup> P. H. Dahl and D. R. Dall'Osto, “Estimation of seabed properties and range from vector  
 748 acoustic observations of underwater ship noise,” *J. Acoust. Soc. Am.* **147**(4), EL345–EL350  
 749 (2020).
- 750 <sup>29</sup> M. Vanneste, C. Madshus, V. L. Socco, M. Maraschini, P. M. Sparrevik, H. Westerdahl,  
 751 K. Duffaut, E. Skomedal, and T. I. Bjørnaraå, “On the use of the Norwegian Geotechnical  
 752 Institute's prototype seabed-coupled shear wave vibrator for shallow soil characterization – I.  
 753 Acquisition and processing of multimodal surface waves,” *Geophys. J. Int.* **185**, 221–236 (2011).
- 754 <sup>30</sup> V. L. Socco, D. Boiero, M. Maraschini, M. Vanneste, C. Madshus, H. Westerdahl, K. Duffaut,  
 755 and E. Skomedal, “On the use of the Norwegian Geotechnical Institute's prototype seabed-  
 756 coupled shear wave vibrator for shallow soil characterization – II. Joint inversion of multimodal  
 757 Love and Scholte surface waves,” *Geophys. J. Int.* **185**, 237–252 (2011).
- 758 <sup>31</sup> S. C. Webb, “Broadband seismology and noise under the ocean,” *Rev. Geophys.* **36**(1), 105–  
 759 142 (1998). doi:10.1029/97RG02287.
- 760 <sup>32</sup> R. A. Stephen, F. N. Spiess, J. A. Collins, J. A. Hildebrand, J. A. Orcutt, K. R. Peal, F. L.  
 761 Vernon, and F. B. Wooding, “Ocean Seismic Network Pilot Experiment,” *Geochem. Geophys.  
 762 Geosyst.* **4**(10), 1092 (2003). doi:10.1029/2002GC000485.
- 763 <sup>33</sup> A. P. Prudnikov, Y. A. Brychkov, and O. I. Marichev, *Integrals and Series, Volume 1:  
 764 Elementary Functions* (Gordon & Breach Sci. Publ., New York, 1986).

- 765 <sup>34</sup> 1. M. Abramovitz and I. A. Stegun (eds.), *Handbook of Mathematical Functions with*  
766 *Formulas, Graphs, and Tables*, Appl. Math. Ser., Vol. 55 (Dover Publications, New York,  
767 1972), pp. 253–293, 555–585.
- 768 <sup>35</sup> K. Aki and P. G. Richards, *Quantitative Seismology*. 2nd edn. (Univ. Science Books,  
769 Sausalito, 2002), pp. 249–254.
- 770 <sup>36</sup> E. L. Hamilton, “Sediment sound velocity measurements made in situ from bathyscaph  
771 Trieste,” *J. Geophys. Res.* **68**(21), 5991–5998 (1963).
- 772 <sup>37</sup> A. J. Duncan, A. N. Gavrilov, R. D. McCauley, I. M. Parnum, and J. M. Collis,  
773 “Characteristics of sound propagation in shallow water over an elastic seabed with a thin cap-  
774 rock layer,” *J. Acoust. Soc. Am.* **134**(1), 207–215 (2013).
- 775 <sup>38</sup> O. A. Godin, N. R. Chapman, M. C. A. Laidlaw, and D. E. Hannay, “Head wave data  
776 inversion for geoacoustic parameters of the ocean bottom off Vancouver Island,” *J. Acoust. Soc.*  
777 *Am.* **106**(5), 2540–2551 (1999).
- 778 <sup>39</sup> J. Li, P. Gerstoft, M. Siderius, and J. Fan, “Inversion of head waves in ocean acoustic ambient  
779 noise,” *J. Acoust. Soc. Am.* **147**(3), 1752–1761 (2020).
- 780